Research Article | Vol. 10, No. 4 | 1 Apr 2019 | BIOMEDICAL OPTICS EXPRESS 1581
Biomedical Optics EXPRESS

Raman spectrum spectral imaging revealing the molecular mechanism of Berberine-induced Jurkat cell apoptosis and the receptor-mediated Berberine delivery system

PING TANG[1], WENDAI CHENG[1], XUANMENG HE[2], QINNAN ZHANG[1], JING ZHONG[1], XIAOXU LU[1], SHENGDE LIU[1], AND LIYUN ZHONG[1]*

[1]*Guangdong Provincial Key Laboratory of Nanophotonic Functional Materials and Devices, South China Normal University, Guangzhou 510006, China*
[2]*Brain academy of South China Normal University, Guangzhou 510631, China*
**zhongly@scnu.edu.cn*

Abstract: Berberine (BBR), a traditional Chinese herb extract medicine, reveals some anticancer effects in leukemia, but it remains controversial about the molecular mechanism of BBR-induced leukemia cell apoptosis. In this study, combining Raman spectrum and spectral imaging, both the biochemical changes of BBR-induced Jurkat cell apoptosis and the precise distribution of BBR in single cell are presented. In contrast, we also show the corresponding results of Jatrorrhizine (JTZ) and Palmatine (PMT), two structural analogues of BBR. It is found that all three structural analogues can induce cell apoptosis by breaking DNA and the main action sites are located in phosphate backbone and base pair groups, but their action on cell cycle are different, in which BBR leads to the S phase arrest while JTZ and PMT are on the G2 phase arrest. Moreover, from the Raman spectra of DNA treated with different drugs, we find that the content of phosphate backbone and base pair groups in BBR-treated DNA are larger than those in JTZ or PMT. And this result reflects the strong capability of BBR breaking DNA backbone relative to JTZ or PMT, suggesting that the existence of methylene-dioxy on the 2, 3 units of A ring on the quinoline ring can greatly enhance the capability of BBR breaking DNA backbone, so the action effect of BBR-induced Jurkat cell apoptosis is better than those of PMT or JTZ. Further, by using Raman spectral imaging approach, we achieve the precise distribution of BBR in single cell, it is found that the receptor-mediated BBR targeting delivery based single-wall carbon nanotube and folic acid (SWNT/FA) reveals excellent performance in BBR targeting delivery relative to the conventional BBR diffusion approach. Importantly, these results demonstrate that Raman spectrum and spectral imaging should be a powerful tool to study the molecular mechanism of drug-induced cell apoptosis and evaluate the efficiency of drug delivery system.

1. Introduction

Berberine (BBR), a natural compound extracted from Chinese herb Coptis chinensis and stable quaternary amine type of isoquinoline alkaloid, has been utilized for diabetes and cardiovascular disease treatment [1,2]. Recent studies show that BBR also can induce some tumor cells (i.e., K562, PC12 and HL60) apoptosis by down-regulating cytokine expression, inhibiting protein synthesis [3–5] and activating the mitochondrial caspase pathway [6]. Specially, it is found that BBR can directly insert into DNA double chain, and then inhibit the activity of topoisomerase I and topoisomerase II, thus induce DNA backbone breaking [7,8], but it remains unknown that which base pairs BBR can intercalate into DNA double helix. In addition, it is reported that Jatrorrhizine (JTZ) and Palmatine (PMT), which are attributed to isoquinoline alkaloid and the structural analogues of BBR (Fig. 1), also reveal anti-tumor effects [9–12], but the corresponding mechanism remains unclear, and the corresponding

#354499 https://doi.org/10.1364/BOE.10.001581
Journal © 2019 Received 7 Dec 2018; revised 30 Jan 2019; accepted 26 Feb 2019; published 4 Mar 2019

Biomedical Optics EXPRESS

biochemical changes of BBR, JTZ and PMT-induced cell apoptosis and their distribution information in single cell are still scarce.

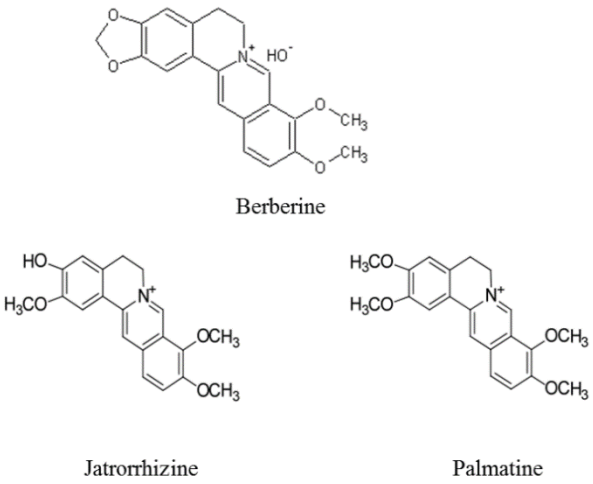

Fig. 1. The structural formula of Berberine, Jatrorrhizine, Palmatine, respectively.

Based on the measurement of the vibration mode of intrinsic molecular bond, Raman spectrum can provide rich bimolecular composition and structural conformation information of single living cell [13–18]. Moreover, due to several specific advantages, such as noninvasive, label-free and real-time, Raman spectrum has been a good candidate for the identification, physical separation and enrichment of living cells [19–21], along with the development of imaging devices, Raman spectral imaging is becoming a potential technique for long-time visualization of biomolecules and drug delivery on single living cell [22–25].

To date, the main treatments of leukemia are chemotherapy and radiotherapy, usually leading to serious damage for normal cell and the side effects. To address this, the drug targeting delivery system is introduced. Carbon nanotubes (CNTs), revealing the advantages of high aspect ratio, high specific surface area, low toxicity and good stability, large loading efficiency, non-immunogenicity, biocompatibility and photoluminescence, is gradually becoming a better solution for drug delivery [26–29].

In this study, by using Raman spectrum and spectral imaging, we hope to achieve the biochemical changes of BBR, JTZ and PMT-induced leukemia cell apoptosis and their distribution information in single cell, and then search for the molecular mechanism of BBR-induced cell apoptosis and the high-performance drug delivery system.

2. Materials and methods

2.1 Cell culture and drug treatment

Jurkat cells, an immortalized line of human T lymphocyte cells that were used to study acute T cell leukemia, were purchased from Medical College of Jinan University (Guangzhou, China). First, Jurkat cells were cultured in medium containing RPMI-1640 medium (Gibco, USA), 10% fetal bovine serum (Gibco, USA), 1% anti-double (penicillin and streptomycin, Holly Corp., USA) in the cell incubator with the temperature of 37°Cand CO2 of 5%. Then, Jurkat cells were seeded in 96-well plates with the density of 1×10^6/ml. Subsequently, BBR (Shanghai Macklin Biochemical, China) with the termhalf maximal effective concentration (EC50) of 18.6uM, which was achieved by the survival rate experiment, JTZ (Aladdin Industrial Corp., China) and PMT (Aladdin Industrial Corp., China) with the same concentration of 18.6uM were added to 96-well plates, respectively. For comparison, three-group samples were prepared as following: Jurkat cells treated with BBR, JTZ and PMT were set as three drug-treated cells.

Biomedical Optics EXPRESS

Similarly, ctDNA (Aladdin Industrial Corp., China) treated with BBR, JTZ and PMT were set as three drug-treated ctDNA. In contrast, Jurkat cells and ctDNA without any treatment were set as the corresponding control groups, respectively. In addition, two stages of cell apoptosis were defined according to the time of drug treatment: (i) in the early stage of cell apoptosis, the drug treatment time was less than 24h; (ii) in the late stage of cell apoptosis, the drug treatment time was more than 48h.

2.2 Raman spectrum and data processing

Micro-Raman spectroscopy (Invia, Renishaw, UK) equipped with an inverted microscope was employed to achieve Raman spectral information of individual Jurkat cell, in which a He-Ne laser with the wavelength of 633nm and maximum output power of 50mw was utilized, a microscope objective with the magnification of 50 × and the corresponding laser spot size on each cell was about 1μm in lateral direction and 2 μm in longitudinal direction. The spectral resolution was 0.99cm^{-1}, due to most of the vibrational spectra of cell biochemical components, such as nucleic acids, lipid, protein, appeared in a fingerprint region of 600 to 1800 cm^{-1}, based on previous studies [15,16,18,19] and aiming at the main biochemical changes of drug-induced Jurkat cell apoptosis, we only presented and analyzed these Raman peaks in the region of 600 to1800 cm^{-1}. For each group samples, more than 20 cells were randomly selected, and for each cell, more than three different areas were selected for spectral measurement; for each Raman spectrum, the exposure time was 10s and the accumulated times is set as three. In Raman spectral imaging, the scanning step length was set as 0.5μm and the acquisition time was 10s for each point.

In our experiment, in order to improve the signal-to-noise ratio of Raman spectrum, the pre-treatment analysis was first implemented with the software package Raman WiRE 4.3, including remove the narrow cosmic rays, correct the base-line and smooth the noise. Subsequently, the area normalization of Raman spectrum, the average spectrum and the spectral difference between Raman spectra were performed with MATLAB R2014a, respectively. Finally, the principal component analysis (PCA) method was chosen to analyze the area normalized Raman spectral data.

2.3 Synthesis of SWNT/FA based BBR targeting delivery system

First, 0.195g 2-[morpholino]ethanesulfonic acid] (MES) and 0.292g NaCl were respectively dissolved in 10ml distilled water and utilized as a buffer solution; 0.008g 1-ethyl-3-[3-dimethylaminopropyl]carbodiimide (EDC) and 0.012g N-hydroxysuccinimide (NHS) were dissolved in 2ml buffer solution, respectively; 25mg folic acid (FA) was added into 250ml distilled water. Second, 1ml EDC and 1ml NHS were respectively added into 5ml FA solution for 2h; meanwhile 1ml EDC and 1ml NHS were added into 10ml SWNT-COOH (~1mg/mL) for 30min, and then above two solutions were mixed together. Third, 20mg amine-polyethylene glycol-amine(H_2N-PEG-NH_2 WM 5000) was added into the mixed solution and incubated for 2h, and centrifuged at 12000rpm for 10min, and then discarded the supernatant and washed with the distilled water, 2ml BBR with the density of 16ug/ml was added for 12h. Finally, the solution was centrifuged at 12000rpm for 10min, so we achieved the SWNT/FA based BBR targeting delivery system.

2.4 Characterization of SWNT based drug delivery system

To evaluate the effectiveness of the synthesized SWNT/FA based BBR delivery system, we employed a UV-vis spectrometer (Agilent 8453) to measure the absorption spectra of four samples (SWNT, SWNT-PEG, SWNT-PEG-FA, SWNT-PEG-FA/BBR), respectively. Moreover, in order to calculate the loading rate of BBR on SWNT, the synthesized SWNT-PEG-FA/BBR was first dissolved with 0.3% Triton solution and stirred overnight, centrifuged. Finally, the supernatant was collected and measured the absorption spectrum.

Biomedical Optics EXPRESS

2.5 Cell viability measurement of SWNT based drug delivery system

To verify cell viability of SWNT based drug delivery system, Jurkat cells were cultured in 96-well plates with the density of 1×10^5/ml, and then BBR with the concentration of 1.6μg/ml, SWNT and SWNT-PEG-FA/BBR with the concentration of 59.2μg/ml were respectively added to 96-well plates and co-cultured for 12h, 24h and 48h. Finally, 10ul of cholecystokinin-octopeptide (CCK-8) solution was added to 96-well plates and was cultured for 2h, and then the absorbance of each well was measured with a microplate reader, thus the corresponding cell viability can be determined.

2.6 Raman spectral imaging of SWNT based drug delivery system

To determine the distribution of SWNT in single cell, we chose the Raman peak at 1586 $cm^{-1,}$ attributed to SWNT, to perform spectral imaging. First, Jurkat cells were cultured in 6-well plates with the density of 1×10^5/ml, 200ul SWNT-PEG-FA/BBR and 200ul SWNT were respectively added to the drug-treated cells and control group for 2h, 6h, 12h, respectively. Subsequently, each group sample were centrifuged, discarded the supernatant, washed, resuspended with PBS, immobilized with polyoxymethylene, and then dropped 20ul on a clean aluminum for Raman spectrum collection and the corresponding spectral imaging.

2.7 Fluorescence imaging and 3D topography

Topographical changes are an essential feature during cell apoptosis. First, Jurkat cells were cultured on 6-well plates with the density of 1×10^5/ml, and then 200ul SWNT-PEG-FA/BBR and 200ul SWNT were added to the drug-treated cells and control group for 2h, 6h, and 12h, respectively. In order to determine whether the cell nucleus changed in drug-induced cell apoptosis, Hoechst 33258, which was a kind of blue nucleic acids fluorescent dye, was employed to stain intracellular nucleus, and then the corresponding fluorescence imaging was achieved with a fluorescence microscope (Nikon Ti-s, Japan). Moreover, three-dimensional (3D) topography of Jurkat cell was recorded by a label-free atomic force microscope (MultiView 4000 AFM Probe, Nanonics, Israel) with nano-scale resolution.

Biomedical Optics EXPRESS

3. Experimental results and discussion

3.1 Evaluation of Jurkat cell apoptosis

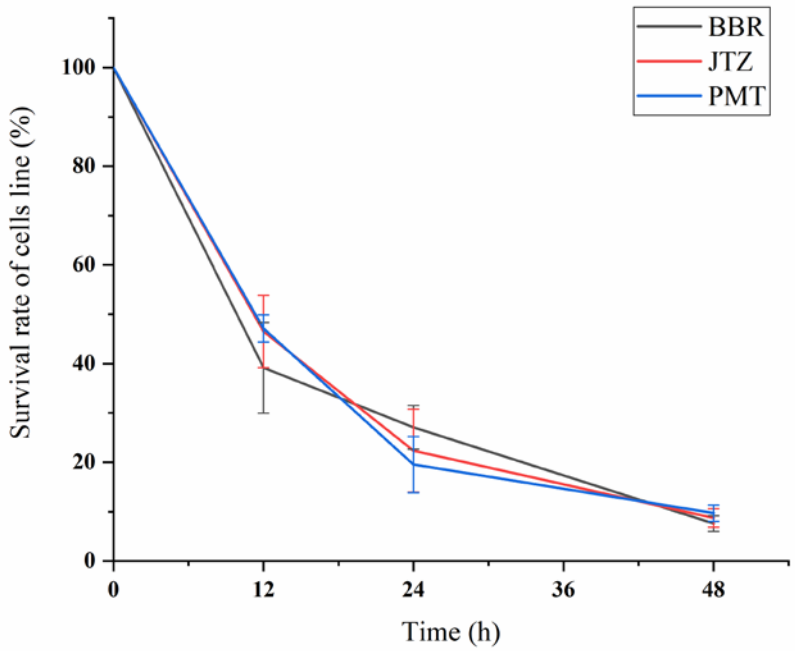

Fig. 2. Survival rate of Jurkat cells treated with BBR, JTZ or PMT, respectively.

In order to evaluate the action effect of drug-induced Jurkat cell apoptosis, we chose cell counting kit-8 (CCK-8) approach to test the toxicity of three drugs, respectively. As shown in Fig. 2, it was found that the survival rates of Jurkat cells treated with BBR, JTZ and PMT for 12h were 39.1%, 46.5% and 47.1%, respectively; for 24h treatment, the corresponding survival rates were decreased to 27.1%, 22.3% and 19.5%, respectively; and for 48h treatment, the survival rates were lower than 10%. These results demonstrated the good action effect of three drug-induced Jurkat cell apoptosis.

Biomedical Optics EXPRESS

3.2 Topographic changes during Jurkat cell apoptosis

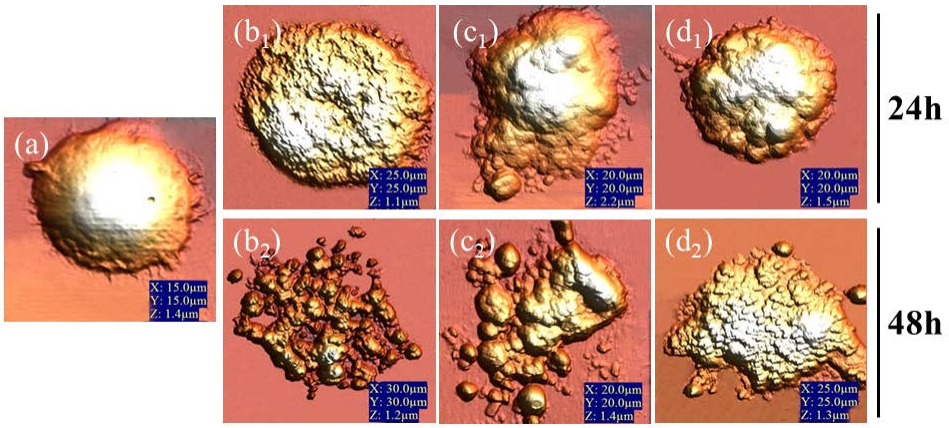

Fig. 3. Topographic images of Jurkat cells (a) without treatment; respectively treated with different drugs for 24h and 48h (b1) (b2) BBR; (c1)(c2) JTZ; (d1)(2) PMT, in which X, Y and Z represented the horizontal, vertical and height scanning ranges, respectively.

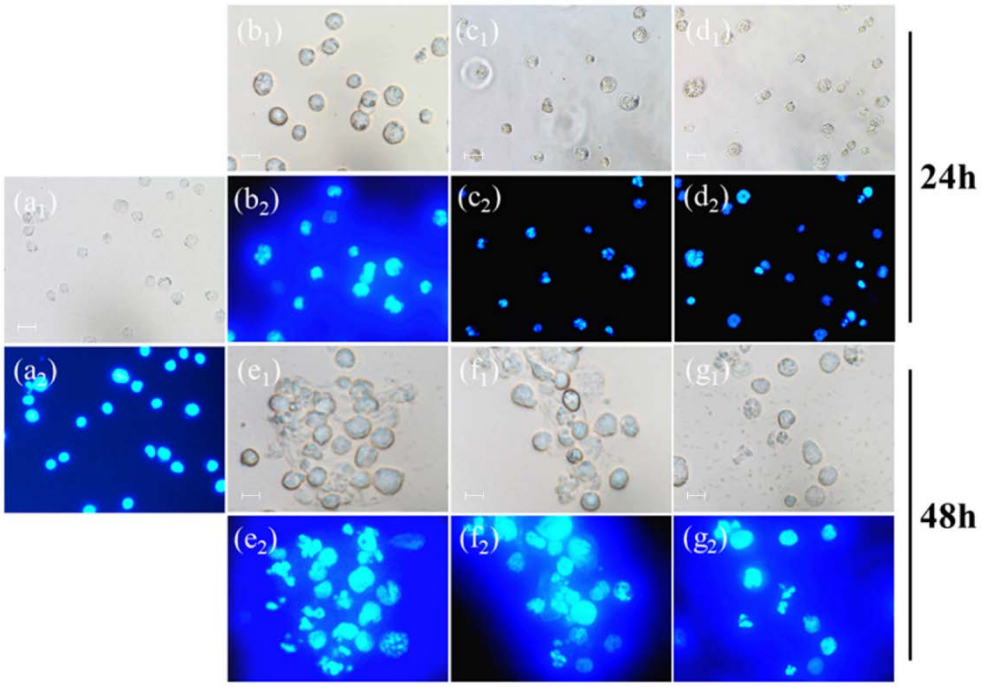

Fig. 4. Bright field images and fluorescent images of Jurkat cells (a1)(a2) without treatment; treated with different drugs for 24h (b1)(b2) BBR; (c1)(c2)JTZ; (d1)(d2) PMT; treated with different drugs for 48h (e1)(e2) BBR; (f1)(f2) JTZ; (g1)(g2) PMT. Scale bar 10 um.

To achieve accurate topographic changes during Jurkat cell apoptosis, an atomic force microscope (AFM) (JPK Nanowarizd, GRE) was employed. As shown in Fig. 3, we can see that the surface of Jurkat cell treated with drugs became rough and the membrane shrinkage appeared, indicating that cell membrane was turned from the intracellular to the extracellular. In contrast, the surface of Jurkat cell without treatment was very smooth. Accordingly, as shown in Fig. 4, the result of cell nucleus staining with Hoechst33342 also demonstrated the good action effects of three drug-induced Jurkat cell apoptosis.

Biomedical Optics EXPRESS

3.3 Raman spectrum analysis of Jurkat cell treated with different drugs

Table 1. Raman peak frequencies and their assignments [13–21,30,31]

Raman frequency(cm^{-1})	Assignment
728	A ring breath
786	U, C, T ring breath., O–P–O str.
826	O–P–O asymmetric str., Tyr ring breath. (p)
938	C = C str.(p)
980	DNA: deoxyribose
1003	Phe ring breath. (p)
1092	O-P = O symmetric str., C-N.(p)
1250	A, T, amide III (p)
1340	A, G, C-H def. (p)
1450	G, A, C-H def. (p),(l)
1575	G, A
1660	Amide I (p), C = C str. (l)

Abbreviations: p, protein; l, lipid; A,G,T,C,U, ring breathing modes of DNA/RNA; str. stretching; breath., breathing; Phe, phenylalanine; Tyr, tyrosine; Trp, tryptophan; def. deformation vibration;

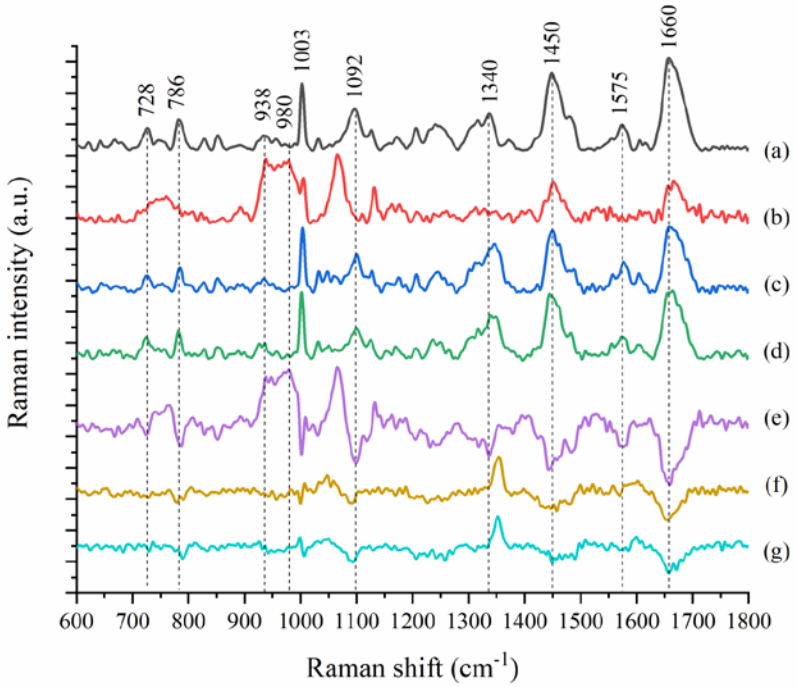

Fig. 5. Average Raman spectra of Jurkat cells (a)without treatment; treated with different drugs for 24h (b)BBR; (c)JTZ; (d) PMT; (e)(f)(g) the spectral differences between (b) (c) (d) and (a), respectively.

Figure 5 showed the average spectra of Jurkat cells without treatment and treated with three drugs for 24h, respectively. Clearly, there were obvious spectral differences between the drug-treated cells and the control group, these peaks at 728, 786, 1092, 1450, 1660cm^{-1} in the drug-treated cells were lower in intensity than those in the control group while the peaks at 938 and 980cm^{-1} in the drug-treated cells were higher than those in the control group. And the interpretation of the Raman data was compared with Table 1, a summary from other studies [13–21,30,31], in which the intensity decreasing of these peaks at 728, 786 and 1092cm^{-1}, respectively attributed to the breathing vibrational mode of adenine A, O-P-O stretching

Biomedical Optics EXPRESS

vibration of DNA backbone and O-P = O vibration of DNA backbone, revealed that drugs had acted on nucleic acids by destroying the structure of phosphodiester bond of DNA skeleton, breaking the phosphate backbone and inhibiting the synthesis of base pairs. The intensity decreasing of these two peaks at 1003 and 1660cm^{-1}, respectively attributed to the breathing vibrational mode of phenylalanine and amide I of protein, reflected that DNA structure was destroyed and the synthesis was inhibited, and the translation and transcriptional procedure of protein were suppressed, thus the content of protein was decreased. The intensity decreasing of the peak at 1450 cm^{-1} was attributed to CH_2 deformation of proteins and lipids. However, the lipids contribution was low relative to the proteins, so the peak at 1450 cm^{-1} should be associated with proteins, further revealing that the drugs also may inhibit proteins synthesis. The peak at 938 cm^{-1}, attributed to the stretching vibration of the protein C-C skeleton, was higher in intensity in BBR-treated group than that in the control group, indicating that BBR also can destroy the structure of protein, disorder the structure of amide I during the transcribed translation, protein skeleton dissociation and aggregation. The intensity increasing of the peak at 980 cm^{-1}, attributed to the ribodesose of DNA, presented that the backbone of DNA was destroyed, so the deoxyribose dissociation and aggregation will lead to the corresponding content increasing. From Figs. 4 (e), 4(f) and 4(g), we can see that the changes of proteins and nucleic acids in BBR-treated cells were larger than those of JTZ or PMT-treated cells, indicating the capability of BBR breaking DNA backbone was stronger than those of JTZ or PMT breaking DNA backbone.

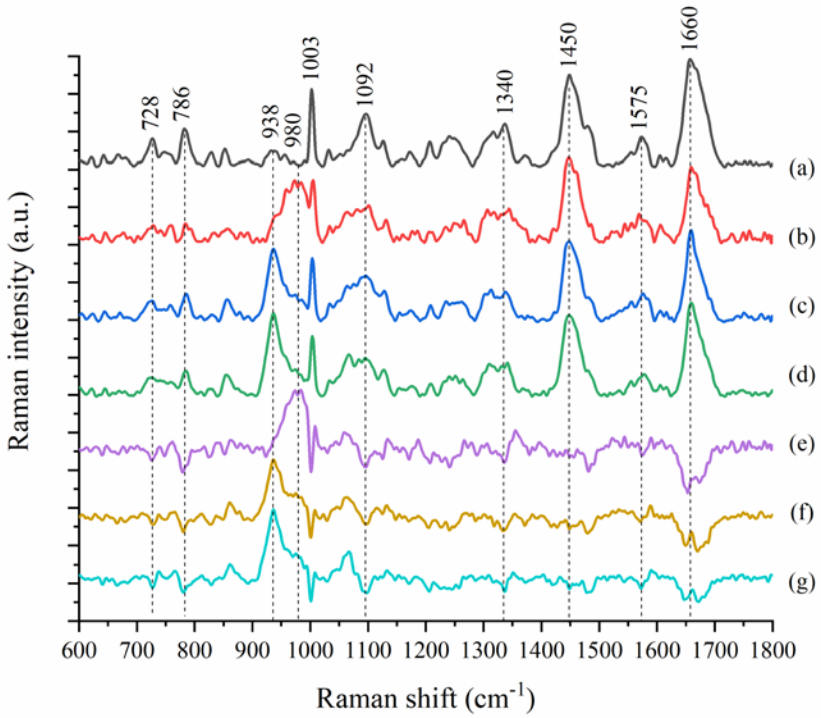

Fig. 6. Average Raman spectra of Jurkat cells (a)without treatment; treated with different drugs for 48h (b)BBR; (c)JTZ; (d)PMT; (e)(f)(g) the spectral differences between (b) (c) (d) and (a), respectively.

Figure 6 showed the average spectra of Jurkat cells without treatment and treated with three drugs for 48h, respectively. The interpretation of Raman data was also compared with Table 1.

Biomedical Optics EXPRESS

We can see that the intensity decreasing of these peaks at 786 and 1092cm^{-1}, attributed to different vibration modes of phosphoric acid skeleton in DNA, further demonstrated that three drugs can subsequently act on the backbone of phosphoric acid, and then break the phosphoric acid skeleton. The intensity decreasing of these peaks at 1003 and 1660cm^{-1}, attributed to the characteristic peaks of proteins, reflected that the content decreasing of DNA also affected the protein synthesis, hinder their transcription and translation. The intensity decreasing of the peak at 1450 cm^{-1}, attributed to the characteristic peak of proteins and lipids, presented that the apoptotic bodies appeared in the late stage of apoptosis, so histones on the chromatin of the nucleus undergo gradual hydrolysis and the cellular membrane was destroyed. The intensity increasing of these peaks at 938 and 980cm^{-1}, respectively attributed to protein C-C skeleton and deoxyribose, showed that the content of protein skeleton was increased and the deoxyribose was dissociated and aggregated.

From the above results, we can conclude that the existence of methylene-dioxy on the 2,3 units of A ring on the quinoline ring will lead to the binding ability decreasing of BBR to proteins, thus the content changes of proteins and nucleic acids in BBR-treated cells were larger than those of JTZ or PMT-treated cells. Therefore, the action effect of BBR-induced Jurkat cell apoptosis was better than those of JTZ or PMT-induced Jurkat cell apoptosis.

3.4 Principal component analysis of Raman spectrum

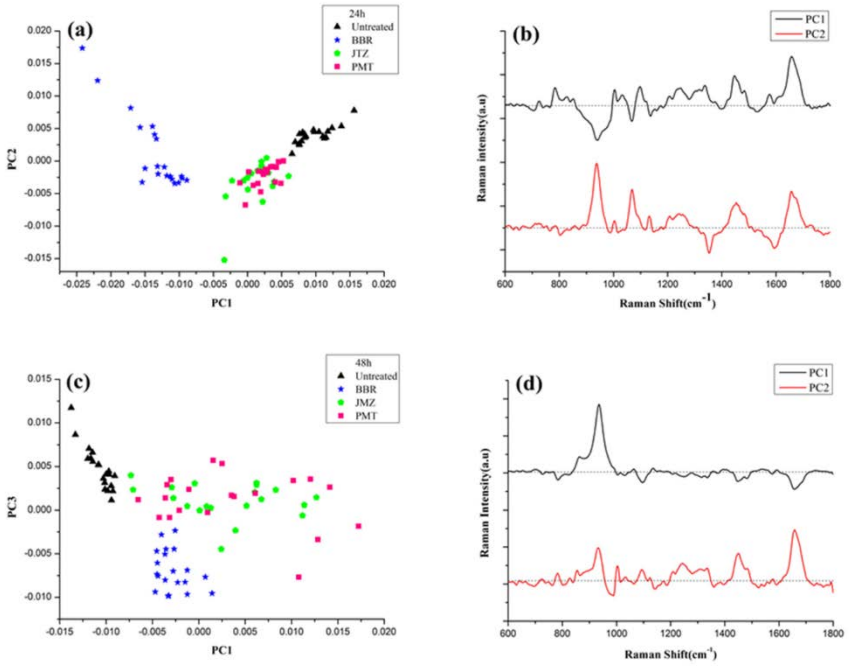

Fig. 7. PCA scatter plots of PC1 and PC2 (or PC3) of Jurkat cells treated with different drugs and the corresponding loading curves during cell apoptosis (a)(b) in the early stage; (c)(d) in the late stage.

Following, in order to carefully compare the spectral differences between different drugs and the contribution of different biochemical components during Jurkat cell apoptosis, we chose PCA multivariate data analysis algorithm [18–20], which is designed to reduce the variable number of a data set and can provide the abstract information representing entire feature broadly distributed in a data set [19], to analyze the collected Raman spectral data. Here, three principal components (PCs) were extracted after the spectral data were mean centered. Figures 7 (a) and (b) showed the scatter plot of PC1 and PC2 and the corresponding loading curves of the first

Biomedical Optics EXPRESS

two PCs of Jurkat cells treated with drugs in the early stage of apoptosis. It was found that contribution of PC1 and PC2 were respectively 48.4% and 12.1%, and note that JTZ-treated cells and PMT-treated cell generated overlapping while BBR-treated cells was separated from them. These peaks at 1003, 1092, 1450, 1660cm^{-1}, respectively attributed to Phe ring breath of protein, O-P = O in DNA backbone, C-H bonds of lipids on cellular membrane, amideI or α-helix of protein, presented the most contribution to PC1. And the peak at 1092cm^{-1} assigned to nucleic acids, these peaks at 1450, 1660cm^{-1} assigned to lipid and the peak at 938cm^{-1} assigned to C-C stretching of protein, showed the most contribution to PC2. Clearly, the above changes of DNA, protein and lipid were greatly related with cell membrane shrinkage in early stage of apoptosis. Moreover, Figs. 6 (c) and 6(d) gave the scatter plot of PC1 and PC2 and the corresponding loading curves of the first two PCs in the late stage of apoptosis, in which the contribution of PC1 and PC2 were 55.9% and 13.5%, respectively. Like the result in early stage of apoptosis, JTZ-treated group and PMT-treated group also generated overlapping while BBR-treated group still was separated from them. These results demonstrated whether in the early or the late stage of apoptosis, the action effect of BBR-treated cells was better than JTZ or PMT-treated cells. Specially, in the late stage of apoptosis, the main biochemical changes came from the protein and lipid, in which the speed of protein synthesis was decreased due to the structure twist of DNA was restrained, so the apoptotic body was observed, meanwhile the content increasing of lipid was accompanied. Accordingly, the peaks at 938cm^{-1} revealed the most contribution to both PC1 and PC2, and these peaks at 1003, 1450 and 1660cm^{-1} had the most contribution for PC2, further indicating that the main spectral difference between BBR-treated cells and JTZ or PMT-treated cells came from the protein and lipid.

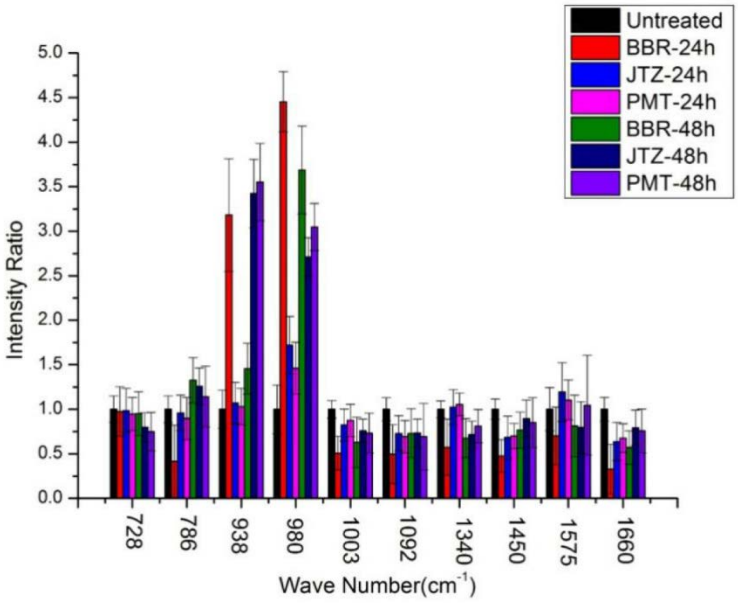

Fig. 8. Intensity variations of selected Raman peaks in the drug-treated cells and the control group, in which the vertical axis was displayed as the intensity ratio of drug-treated cells to the control group.

C ollectively, by combining PCA multivariate data analysis and intensity variations of the key spectral peak as shown in Fig.8, we achieved the biochemical changes of BBR-induced Jurkat cell apoptosis. we can see although there were small structural difference between BBR and JTZ or PMT, but the action effect of BBR-induced Jurkat cell apoptosis was better than those of PMT or JTZ, suggesting the main reasons are as following: First, due to the existence of methylene-dioxy of A ring, BBR cannot only enhance the inhibitory activity against

Biomedical Optics EXPRESS

topoisomerase II [7,32] and binding ability to Bcl-2 protein [33], but also generate complexes with telomeric G-four DNA and telomeric double stranded DNA while PMT and JTZ generated complexes only with the telomeric G-four DNA [34]. Second, BBR mainly performed on S phase of Jurkat cell, in which the replication of DNA was ended and the corresponding content was increased. In contrast, JTZ and PMT performed on G2 phase arrest, in which the replication of DNA was ended but the synthesis of protein was still performed. Third, although BBR, JTZ and PMT can destroy the skeleton of phosphoric acid, but their action way was different, in which BBR was performed through the electrostatic attraction to bind phosphate backbone skeleton, and then destroyed the phosphoric acid skeleton of DNA, so the content of phosphoric acids was decreased. In addition, by inserting into base pairs of the quinoline ring, BBR will break the hydrogen bonds between A-T and C-G, and then the deoxyribose was dissociated, thus the content of hydrogen bonds was decreased while the content of deoxyribose was increased. In contrast, although both JTZ and PMT can destroy DNA structure by the binding way, the ribodesose and histone were dissociated and accumulated, so the corresponding contents were increased during whole Jurkat cell apoptosis. As a result, the action effect of BBR-induced cell apoptosis was better than those of JTZ or PMT whether in the early stage of apoptosis or in the late stage of apoptosis. Importantly, the achieved result also showed that BBR-induced Jurkat cell apoptosis was performed rapidly by destroying DNA phosphoric acid skeleton and then changing protein structure, but JTZ or PMT-induced Jurkat cell apoptosis was implemented slowly by changing protein structure then destroying DNA phosphoric acid skeleton. Therefore, we can see that BBR induces cell apoptosis mainly by destroying DNA in the nucleus.

Biomedical Optics EXPRESS

3.5 Raman spectral imaging during Jurkat cell apoptosis

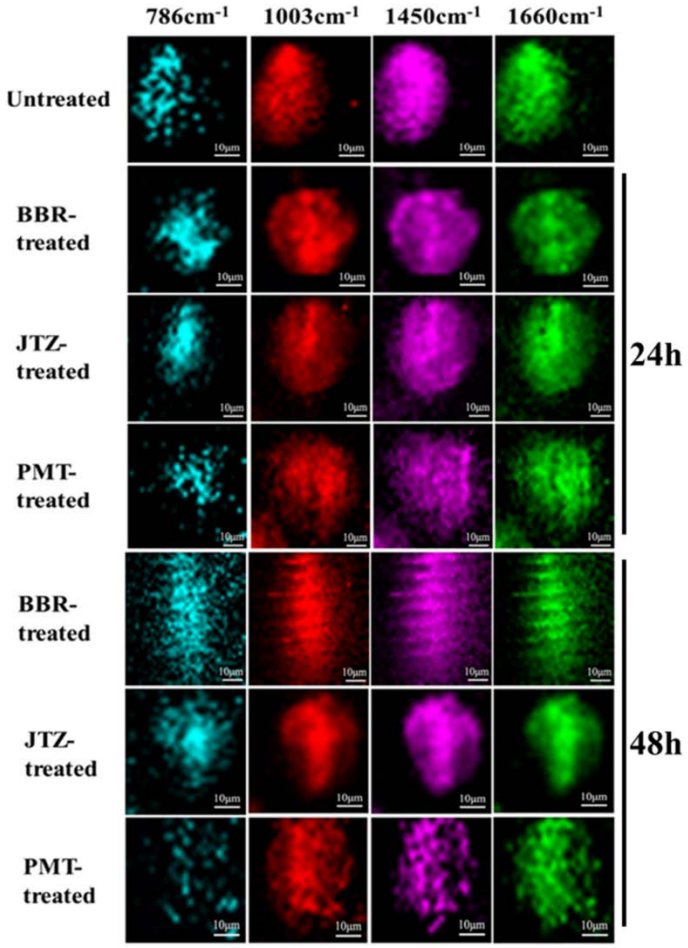

Fig. 9. Raman spectral imaging result of Jurkat cells treated with different drugs

Along with the development of imaging devices, Raman spectral imaging is becoming a potential technique for long-time visualization of biomolecules and drug delivery in single cell. In this section, we employed Raman spectral imaging to achieve the precise distribution of biochemical components during Jurkat cell apoptosis. Figure 9 showed the Raman spectral imaging result of Jurkat cells without treatment and treated with different drugs, in which four characteristic Raman peaks at 786, 1003, 1450, 1660cm^{-1}, assigned to O-P-O in nucleic acids, Phe ring breath of protein, C-H bonds of lipid, amideIor α-helix of protein, were chosen to achieve imaging, respectively. We can see that in the control group, the distribution of nucleic acids were dispersive while the distribution of protein and lipid were relatively concentrated. In contrast, in the BBR-treated cell, the distribution of nucleic acids became concentrated, indicating that the chromatin pyknosis appeared; the distribution changes of protein and lipid were not obvious, reflecting that the nucleic acids should be the main action sites of BBR. Accordingly, the result of JTZ-treated cells was similar to BBR-treated cells. For PMT-treated cells, the distributions of all peaks imaging were dispersive, indicating that the action of PMT affected not only nucleic acids but also protein and lipid. In addition, we can see that in the latter stage of apoptosis, the distribution of nucleic acids became disperse relative to the early stage, indicating that the drugs sustainedly acted on O-P-O of DNA. As a result, the nucleus

Biomedical Optics EXPRESS

fragmentation appeared and the content of DNA was decreased. In contrast, the content of protein and lipid in BBR-treated cells or JTZ-treated cells were low relative to PMT-treated group. Importantly, the good dispersity of protein and lipid in PMT-treated cells further demonstrated that PMT may sustainedly act on protein and lipid during whole cell apoptosis.

3.6 Raman spectrum of DNA treated with different drugs

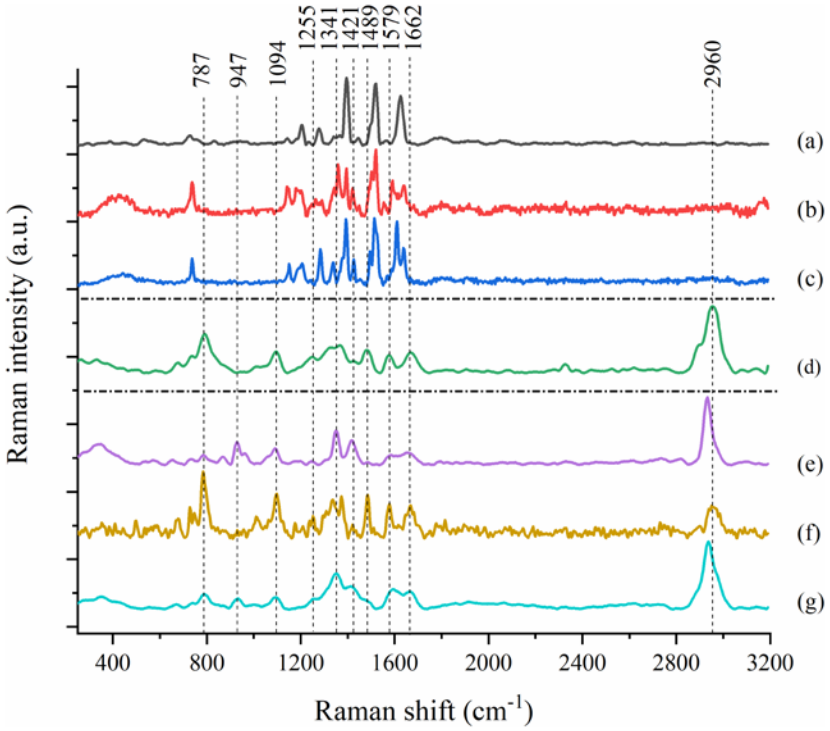

Fig. 10. Average Raman spectra of different drugs (a)BBR; (b)JTZ; (c)PMT; average Raman spectra of DNA (d)without treatment, treated with different drugs (e)BBR; (f)JTZ; (g)PMT, respectively.

Table 2. Raman peak frequencies and their assignments [14–18,31]

Raman frequency(cm^{-1})	Assingment
787	O-P-O two ester symmetrical stretching
947	Deoxyribose ring breath
1094	O = P-O symmetric expansion
1255	A: ring breath.
1341	A: ring breath
1421	A,G: ring breath
1489	G: ring breath
1579	G,A: ring breath.
1662	hydrogen bond
2960	Deoxyribose ring breath

Abbreviations: A-adenine; G-Guanine; C-cytosine; T-Thymine.

To further search for accurate action sites of drugs on DNA double helix, Fig. 10 gave the average Raman spectra of DNA treated with different drugs, as well as the corresponding spectral difference. The interpretation of DNA Raman data was compared with Table 2, a summary from other studies [14-18, 31]. We can see that in BBR or PMT-treated DNA for 48 h, the obvious intensity decreasing of DNA peak at 787 cm^{-1} revealed that the phosphodiester bond of DNA was destroyed. The intensity increasing of peak at 947 cm^{-1} presented that deoxyribose was dissociated from DNA and then aggregated, and the intensity decreasing of

Biomedical Optics EXPRESS

peak at 1094 cm^{-1} reflected that the phosphodiester bond was broken. The intensity decreasing of peak at 1489 and 1579 cm^{-1} showed the weakening of CG base vibration, indicating that the structure DNA was destroyed. Note that the significant intensity increasing of peaks at 1255, 1341 and 1421 cm^{-1} showed that AT base pairs were destroyed, base A was free from DNA and then aggregated, one vibration peak appeared. The intensity decreasing of peak at 1662 cm^{-1} revealed that the hydrogen bond in DNA was destroyed, and the intensity decreasing of peak at 2960 cm^{-1} presented that the pentosan was partly destroyed. In addition, in JTZ-treated DNA for 48 h, no significant changes in most peaks of DNA while the peaks at 787 and 1094 cm^{-1} were increased and the peak at 2960 cm^{-1} was decreased in intensity. This result demonstrated that the action sites of JTZ in DNA were located in the phosphoric acid skeleton and pentose while the action sites of BBR and PMT in DNA mainly were located in the phosphodiester bond, hydrogen bond and AT base pair. That is to say, the action sites of BBR were the phosphate backbone and base pair groups, so the action effect of BBR and PMT in DNA was better than that of JTZ. Importantly, we can see in BBR-treated DNA, the peak at 1094 cm^{-1}, attributed to O = P = O, had a slight blue-shift to 1088cm^{-1}, indicating that DNA double strands was fractured. And the peak at 787cm^{-1}, assigned to O-P-O stretching vibration, appeared red-shift to 791cm^{-1}, reflecting the disorder of DNA double helix structure, meanwhile the corresponding intensity decreasing further demonstrated that the double strands of DNA were broken. In contrast, in JTZ or PMT-treated DNA, the peak at 787cm^{-1} appeared blue-shift while their Raman spectra were similar to that of BBR-treated DNA. In a word, though both JTZ and PMT can destroy DNA by inserting the phosphate acid backbone and hydrogen bond, but their action effect was weaker than that of BBR, suggesting the reason was that the existence of methylene-dioxy on the 2,3 units of A ring on the quinoline ring of BBR will lead to the strong steric effect, and then enhance the capability of BBR breaking DNA backbone.

3.7 Characterization of SWNT/FA based BBR targeting delivery system

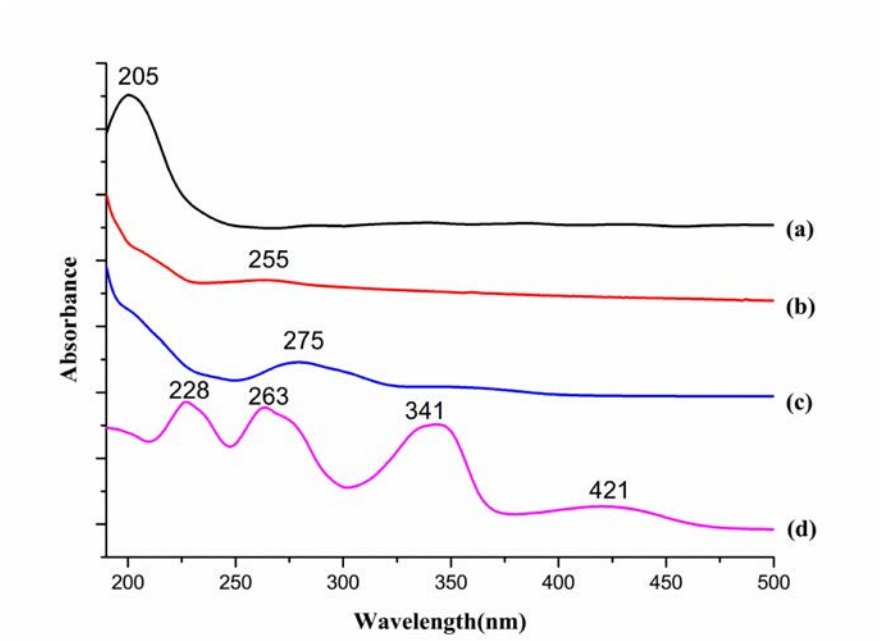

Fig. 11. The UV-vis absorption spectra of SWNT conjugated with different carriers (a)SWNT;(b) SWNT-PEG;(c) SWNT-PEG-FA;(d) SWNT -PEG-FA/BBR

Biomedical Optics EXPRESS

To search for the effective solution of BBR targeting delivery, we designed and prepared a single-wall carbon nanotube (SWNT) based folic acid (SWNT/FA) receptor-mediated BBR delivery system. Figure 11 showed the UV-vis absorption spectra of SWNT conjugated with different carriers. We can see that SWNT has the maximum absorption peak at 205nm; and in SWNT-PEG, one weak absorption peak at 255nm, assigned to PEG, was observed, the intensity decreasing of peak at 205nm and the peak appearance of PEG demonstrated that PEG was successfully conjugated with SWNT. In SWNT-PEG-FA, one absorption peak at 275nm appeared, indicating that the SWNT-PEG was successfully conjugated with FA. In SWNT-PEG-FA/BBR, these peaks at 228, 263, 341, and 421nm, assigned to BBR, were observed, showing that BBR has been conjugated to the SWNT-PEG-FA carrier.

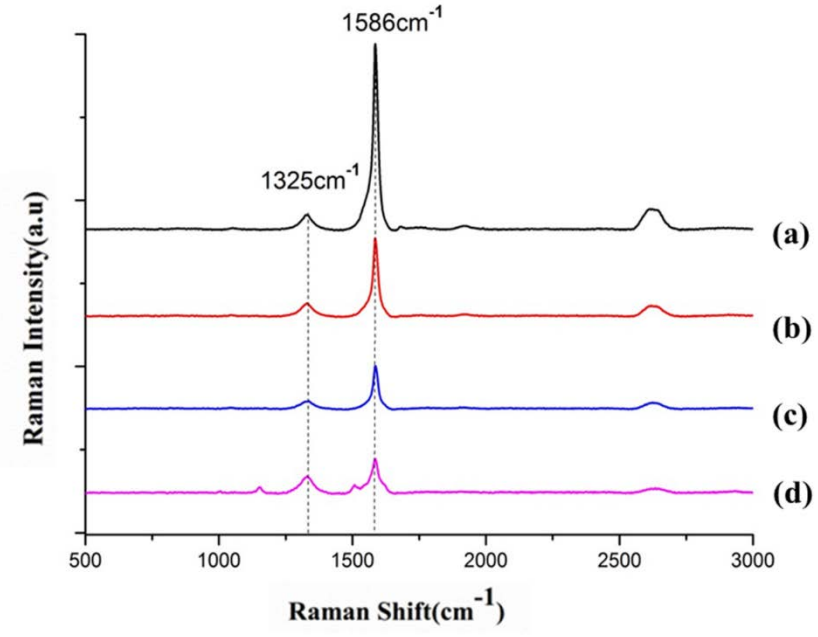

Fig. 12. Raman spectra of SWNT conjugated with different number carriers (a)SWNT;(b) SWNT-PEG;(c) SWNT-PEG-FA;(d) SWNT-PEG-FA/BBR

Further, Fig. 12 gave Raman spectral changes of SWNT conjugated with different number carriers. Clearly, one strong characteristic Raman peak of SWNT at 1586cm^{-1}, attributed to G band of SWNT, and one weak Raman peak at 1325cm^{-1}, attributed to the D band of SWNT, were observed. In general, the peak intensity ratio of I_D/I_G is employed to present the defect number. We can see the along with the number increasing of conjugated carriers (from SWNT to PEG, FA and BBR), the ratio value of I_D/I_G was gradually increased. This result further demonstrated that the carriers of PEG, FA, and BBR were successfully conjugated to SWNT step by step, that is to say, the SWNT/FA based BBR targeting delivery system have been synthesized successfully.

Biomedical Optics EXPRESS

3.8 The loading rate of SWNT-PEG-FA/BBR

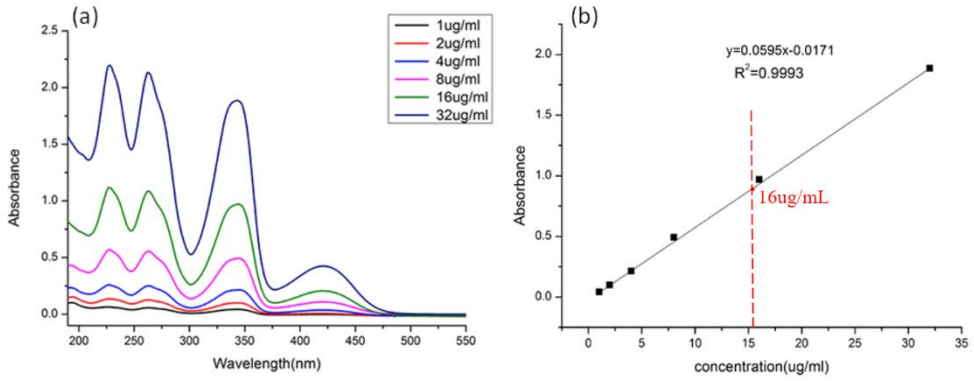

Fig. 13. (a) UV-Vis absorption spectra variation of the prepared SWNT-PEG-FA/BBR with the BBR concentration; (b)the fitting curve of the absorbance with the BBR concentration. The dotted red line is 16 ug/mL.

Figure 13 presented that the absorption spectra of SWNT based BBR delivery system. We can see that along with the concentration increasing of BBR solution, the peak intensity was linearly increased ($y = 0.0595x-0.0171$, $R^2 = 0.9993$), indicating the prepared SWNT-PEG-FA/BBR sample was suitable for BBR targeting delivery [26], and then inducing cell apoptosis. Further, we chose the concentration 16ug/mL of BBR to determine 2.7% loading rate of SWNT to BBR.

3.9 The survival rate of Jurkat cells treated with different carriers

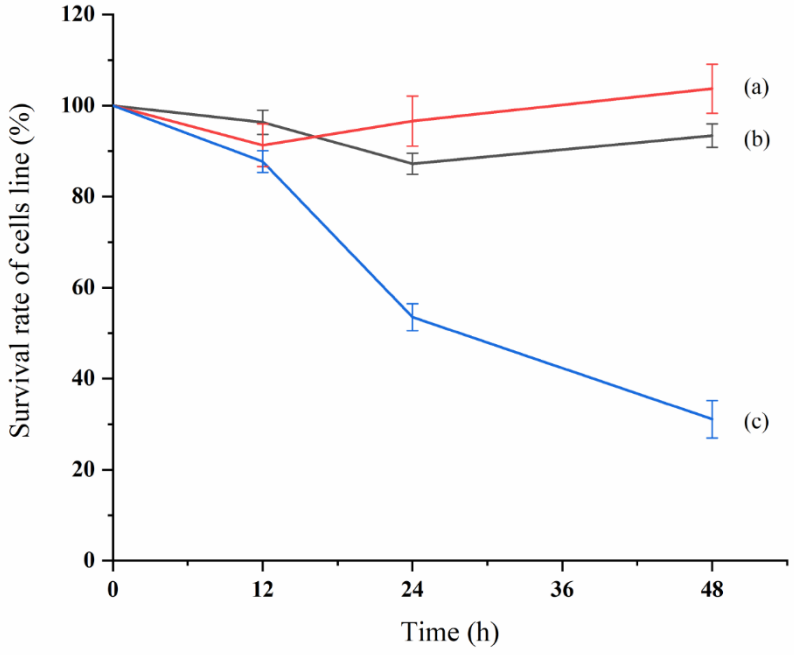

Fig. 14. Survival rate of Jurkat cells treated with different carriers (a) SWNT;(b)BBR;(c) SWNT-PEG-FA/BBR

Biomedical Optics EXPRESS

To verify the cytotoxicity of individual SWNT and the synthesized SWNT-PEG-FA/BBR, Fig. 14 showed the survival rate of Jurkat cells treated with different carriers. It was found that for 12h treatment, the survival rates of Jurkat cells treated with BBR, SWNT and SWNT-PEG-FA/BBR were respectively 96.3%, 91.3%, 87.7%; for 24h treatment, the corresponding survival rates were 87.2%, 96.6% and 53.5%; for 48h treatment, the corresponding survival rates were 93.4%, 103.7% and 31.1%. These results demonstrated that the SWNT based FA receptor-mediated system was a very suitable for BBR targeting delivery and therapy.

3.10 Visualization of cell uptake SWNT-PEG-FA/BBR

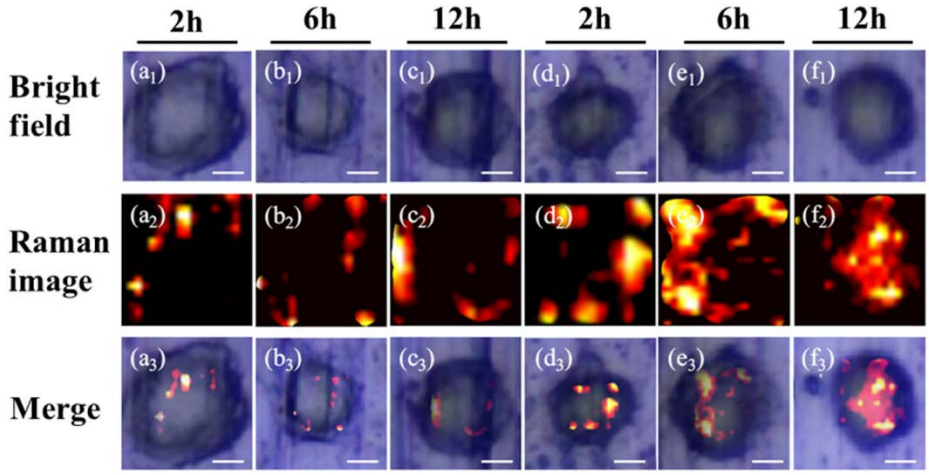

Fig. 15. Raman spectral imaging results during Jurkat cell uptake individual SWNT or synthesized SWNT-PEG-FA/BBR (a1)(a2)(a3)SWNT for 2h; (b_1)(b2)(b_3)SWNT for 6h; (c_1)(c2)(c_3)SWNT for 12h; (d1)(d2)(d3)SWNT-PEG-FA/BBR for 2h; (e_1)(e2)(e_3) SWNT-PEG-FA/BBR for 6h; (f_1)(f2)(f_3) SWNT-PEG-FA/BBR for 12h; in which the 1st, 2nd, 3rd rows respectively denoted the bright field image, magnified Raman image and Merge image (scale bar 2μm).

To present the advantage of the synthesized SWNT-PEG-FA/BBR delivery system, we performed the Raman spectral imaging of Jurkat cell uptake SWNT and SWNT-PEG-FA/BBR, respectively, in which the Raman peak of SWNT at 1586cm^{-1} was chosen to achieve spectral imaging, as shown in Fig. 15. We can see that the amount of intracellular SWNT in SWNT-treated cell was less than that of SWNT-PEG-FA/BBR-treated cell, and in the former, the SWNT still mainly distributed in cell membrane, reflecting the amount of cellular uptake SWNT was small by the conventional diffusion approach. However, in the latter, the amount of cellular uptake SWNT-PEG-FA/BBR was greatly increased and concentrated on cell nucleus, indicating that the FA receptor-mediated Jurkat cell uptake was very effective for BBR targeting delivery and therapy. Importantly, this Raman spectral imaging will supply a powerful tool to study the molecular mechanism of drug-induced cell apoptosis and the efficiency of drug delivery system.

Biomedical Optics EXPRESS

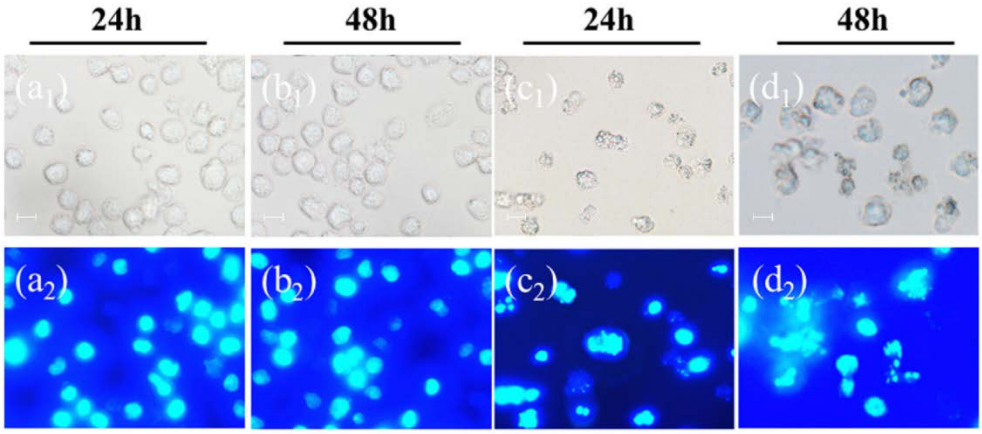

Fig. 16. Bright field and fluorescence images of Jurkat cells treated with (a_1)(a_2), (b_1)(b_2) BBR; (c_1)(c_2), (d_1)(d_2) SWNT-PEG-FA/BBR (bar:10 um).

For comparison, Fig. 16 also gave that bright field and fluorescence images of Jurkat cells treated with BBR and SWNT-PEG-FA/BBR, respectively. It was found that action effect of SWNT-PEG-FA/BBR-induced Jurkat cell apoptosis was significantly better than that of BBR, further revealing the outstanding performance of SWNT/FA receptor-mediated BBR targeting delivery approach relative to the conventional BBR diffusion approach.

4. Conclusion

In this study, by combining Raman spectra and PCA, the biochemical changes of three structural analogues (BBR, JTZ and PMT)-induced Jurkat cell apoptosis were presented. It is found that all three structural analogues can induce cell apoptosis by breaking DNA and the main action sites are located in phosphate backbone and base pair groups, but their action on cell cycle are different, in which BBR leads to the S phase arrest while JTZ and PMT are on the G2 phase arrest. Moreover, the Raman spectra of DNA treated with different drugs present that the content changes of phosphate backbone and base pair groups in BBR-treated DNA are larger than those in JTZ-treated or PMT-treated DNA, indicating the capability of BBR breaking DNA backbone is stronger than those of JTZ or PMT,. Further, one receptor-mediated BBR targeting delivery system based on SWNT/FA was designed and prepared, and by using Raman spectral imaging, we achieved the precise distribution information of BBR in single cell. Compared with the conventional BBR diffusion approach, the SWNT/FA based receptor-mediated system revealed excellent performance in BBR targeting delivery and the corresponding action effect. Importantly, above results demonstrate that Raman spectrum and spectral imaging should be a powerful tool to study the molecular mechanism of drug-induced cell apoptosis and the efficiency of drug delivery system.

Funding

National Nature Science Foundation of China (grants: 61575069, 61875059 and 61727814).

Disclosures

The authors declare that there are no conflicts of interest related to this article.

References

1. G. H. Lu, L. M. Wang, and J. M. Chen, “Determination and utilization of berberine in plants of Berberis L,” J. Chin. Tradit. Herbal Drugs **30**(6), 428–430 (1999).
2. S. H. Xu, M. S. He, and X. P. Liu, “Berberine contents on B. triacanthophora,” J Chin Med Mater **26**(3), 183–184 (2003).

Biomedical Optics EXPRESS

3. Y. Wang, M. M. Kheir, Y. Chai, J. Hu, D. Xing, F. Lei, and L. Du, "Comprehensive study in the inhibitory effect of berberine on gene transcription, including TATA box," PLoS One **6**(8), e23495 (2011).
4. Y. Pazhang, S. Ahmadian, M. Mahmoudian, and M. Shafiezadeh, "Berberine-induced apoptosis via decreasing the survivin protein in K562 cell line," Med. Oncol. **28**(4), 1577–1583 (2011).
5. H. L. Wu, C. Y. Hsu, W. H. Liu, and B. Y. Yung, "Berberine-induced apoptosis of human leukemia HL-60 cells is associated with down-regulation of nucleophosmin/B23 and telomerase activity," Int. J. Cancer **81**(6), 923–929 (1999).
6. J. M. Hwang, H. C. Kuo, T. H. Tseng, J. Y. Liu, and C. Y. Chu, "Berberine induces apoptosis through a mitochondria/caspases pathway in human hepatoma cells," Arch. Toxicol. **80**(2), 62–73 (2006).
7. Y. Kobayashi, Y. Yamashita, N. Fujii, K. Takaboshi, T. Kawakami, M. Kawamura, T. Mizukami, and H. Nakano, "Inhibitors of DNA topoisomerase I and II isolated from the Coptis rhizomes," Planta Med. **61**(5), 414–418 (1995).
8. S. Letasiová, S. Jantová, M. Miko, R. Ovádeková, and M. Horváthová, "Effect of berberine on proliferation, biosynthesis of macromolecules, cell cycle and induction of intercalation with DNA, dsDNA damage and apoptosis in Ehrlich ascites carcinoma cells," J. Pharm. Pharmacol. **58**(2), 263–270 (2006).
9. T. X. Wang and X. H. Yang, "Reversal effect of isotetrandrine, an isoquinoline alkaloid extracted from Caulis Mahoniae, on P-glycoprotein-mediated doxorubicin-resistance in human breast cancer (MCF-7/DOX) cells," Yao Xue Xue Bao **43**(5), 461–466 (2008).
10. H. G. Hambright, I. S. Batth, J. Xie, R. Ghosh, and A. P. Kumar, "Palmatine inhibits growth and invasion in prostate cancer cell: Potential role for rpS6/NFκB/FLIP," Mol. Carcinog. **54**(10), 1227–1234 (2015).
11. J. Wu, Q. Xiao, N. Zhang, C. Xue, A. W. Leung, H. Zhang, Q. J. Tang, and C. Xu, "Palmatine hydrochloride mediated photodynamic inactivation of breast cancer MCF-7 cells: Effectiveness and mechanism of action," Photodiagn. Photodyn. Ther. **15**, 133–138 (2016).
12. R. Liu, Z. Cao, Y. Pan, G. Zhang, P. Yang, P. Guo, and Q. Zhou, "Jatrorrhizine hydrochloride inhibits the proliferation and neovascularization of C8161 metastatic melanoma cells," Anticancer Drugs **24**(7), 667–676 (2013).
13. G. J. Puppels, F. F. de Mul, C. Otto, J. Greve, M. Robert-Nicoud, D. J. Arndt-Jovin, and T. M. Jovin, "Studying single living cells and chromosomes by confocal Raman microspectroscopy," Nature **347**(6290), 301–303 (1990).
14. W. L. Peticolas, "Raman spectroscopy of DNA and proteins," Methods Enzymol. **246**, 389–416 (1995).
15. R. Buckmaster, F. Asphahani, M. Thein, J. Xu, and M. Zhang, "Detection of drug-induced cellular changes using confocal Raman spectroscopy on patterned single-cell biosensors," Analyst (Lond.) **134**(7), 1440–1446 (2009).
16. G. B. Jung, Y. J. Lee, G. Lee, and H. K. Park, "A simple and rapid detection of tissue adhesive-induced biochemical changes in cells and DNA using Raman spectroscopy," Biomed. Opt. Express **4**(11), 2673–2682 (2013).
17. D. W. Shipp, F. Sinjab, and I. Notingher, "Raman spectroscopy: techniques and applications in the life sciences," Adv. Opt. Photonics **9**(2), 315 (2017).
18. G. B. Jung, J. E. Huh, H. J. Lee, D. Kim, G. J. Lee, H. K. Park, and J. D. Lee, "Anti-cancer effect of bee venom on human MDA-MB-231 breast cancer cells using Raman spectroscopy," Biomed. Opt. Express **9**(11), 5703–5718 (2018).
19. J. W. Chan, D. K. Lieu, T. Huser, and R. A. Li, "Label-free separation of human embryonic stem cells and their cardiac derivatives using Raman spectroscopy," Anal. Chem. **81**(4), 1324–1331 (2009).
20. H. J. Byrne, F. Bonnier, A. Casey, M. Maher, J. McIntyre, E. Efeoglu, and Z. Farhane, "Advancing Raman microspectroscopy for cellular and subcellular analysis: towards in vitro high-content spectralomic analysis," Appl. Opt. **57**(22), E11–E19 (2018).
21. J. Gala de Pablo, F. J. Armistead, S. A. Peyman, D. Bonthron, M. Lones, S. Smith, and S. D. Evans, "Biochemical fingerprint of colorectal cancer cell lines using label-free live single-cell Raman spectroscopy," J. Raman Spectrosc. **49**(8), 1323–1332 (2018).
22. S. Stewart, H. Kirschner, P. J. Treado, R. Priore, M. Tretiakova, and J. K. Cohen, "Distinguishing between renal oncocytoma and chromophobe renal cell carcinoma using Raman molecular imaging," J. Raman Spectrosc. **45**(4), 274–280 (2014).
23. C. Krafft, M. Schmitt, I. W. Schie, D. Cialla-May, C. Matthäus, T. Bocklitz, and J. Popp, "Label-Free Molecular Imaging of Biological Cells and Tissues by Linear and Nonlinear Raman Spectroscopic Approaches," Angew. Chem. Int. Ed. Engl. **56**(16), 4392–4430 (2017).
24. B. Prats Mateu, E. Harreither, M. Schosserer, V. Puxbaum, E. Gludovacz, N. Borth, N. Gierlinger, and J. Grillari, "Label-free live cell imaging by Confocal Raman Microscopy identifies CHO host and producer cell lines," Biotechnol. J. **12**(1), 1600037 (2017).
25. P. Heraud, M. F. Cowan, K. M. Marzec, B. L. Møller, C. K. Blomstedt, and R. Gleadow, "Label-free Raman hyperspectral imaging analysis localizes the cyanogenic glucoside dhurrin to the cytoplasm in sorghum cells," Sci. Rep. **8**(1), 2691 (2018).
26. R. Li, R. Wu, L. Zhao, Z. Hu, S. Guo, X. Pan, and H. Zou, "Folate and iron difunctionalized multiwall carbon nanotubes as dual-targeted drug nanocarrier to cancer cells," Carbon **49**(5), 1797–1805 (2011).
27. Q. Guo, X. T. Shen, Y. Y. Li, and S. Q. Xu, "Carbon nanotubes-based drug delivery to cancer and brain," J. Huazhong Univ. Sci. Technolog. Med. Sci. **37**(5), 635–641 (2017).

Biomedical Optics EXPRESS

28. N. K. Mehra and N. K. Jain, "Multifunctional hybrid-carbon nanotubes: new horizon in drug delivery and targeting," J. Drug Target. **24**(4), 294–308 (2016).
29. S. Kaura, N. K. Mehraa, K. Jaina, N. K. Jain, "Development and evaluation of targeting ligand-anchored CNTs as prospective targeted drug delivery system" J. Taylor & Francis, 2169–141X (Online) (2016).
30. P. Liu, J. H. Li, Z. W. Tu, Z. Y. Guo, Z. F. Zhuang, and Y. F. Xia, "Discrimination of NPC cell lines associated with malignant types using Raman spectroscopy," J. Laser Phys. **22**(11), 1682–1688 (2012).
31. K. le Roux, L. C. Prinsloo, A. A. Hussein, and N. Lall, "A micro-Raman spectroscopic investigation of leukemic U-937 cells treated with Crotalaria agatiflora Schweinf and the isolated compound madurensine," Spectrochim. Acta A Mol. Biomol. Spectrosc. **95**(5), 547–554 (2012).
32. P. Krishnan and K. F. Bastow, "The 9-position in berberine analogs is an important determinant of DNA topoisomerase II inhibition," Anticancer Drug Des. **15**(4), 255–264 (2000).
33. Y. X. Zhang, X. F. Zhang, and Y. L. Tang, "Studies of the Interactions between Three Protoberberine Alkaloids and Bcl-2 by Fluorescence Spectroscopy," J. Acta Chimica Sinica **69**(2), 247–251 (2011).
34. M. Franceschin, L. Rossetti, A. D'Ambrosio, S. Schirripa, A. Bianco, G. Ortaggi, M. Savino, C. Schultes, and S. Neidle, "Natural and synthetic G-quadruplex interactive berberine derivatives," Bioorg. Med. Chem. Lett. **16**(6), 1707–1711 (2006).